DESIGN OF A HYBRID-TYPE SHORT-SPAN SELF-BEARING MOTOR

Seung-Jong Kim
Satellite Venture Business Lab., Ibaraki University, Hitachi, Ibaraki Pref., Japan
sjkim@mech.ibaraki.ac.jp
Tatsunori Shimonishi
Dept. of Mechanical Eng., Ibaraki University, Hitachi, Ibaraki Pref., Japan
Hideki Kanebako
Dept. of Mechanical Eng., Ibaraki University, Hitachi, Ibaraki Pref., Japan
hideki.kanebako@sankyoseiki.co.jp
Yohji Okada
Dept. of Mechanical Eng., Ibaraki University, Hitachi, Ibaraki Pref., Japan
okada@mech.ibaraki.ac.jp

ABSTRACT
In this paper, a self-bearing motor is newly proposed for the application to an artificial heart pump. The motor consists of two functions using a stator in common; one part is a general permanent magnet (PM) motor and the other is the so-called hybrid active magnetic bearing (AMB). An outer rotor is actively controlled only in two radial directions while the other motions are passively stable owing to the short-span structure. Main advantages of this hybrid-type self-bearing motor are low power consumption, simple control mechanism and smart structure. A mathematical model for the hybrid AMB part is built with consideration of the radial movement of the rotor. The model helps us not only to design a levitation controller but also to expect the system performance. Some experimental results show the feasibility of the proposed self-bearing motor for use in the artificial heart.

INTRODUCTION
According to the increase of application fields of AMB systems, e.g. an artificial heart, new need of a small-sized AMB-motor system has arisen. Hence, a self-bearing motor has drawn much attention among many researchers. The self-bearing motors [1-3] have the combined function of a motor and an AMB, so that a rotor could be magnetically supported while rotating. Although these previous self-bearing motors worked well and had sufficient performance, they disclosed some complications in the control mechanism and also in the structure. To improve the drawbacks, a hybrid-type self-bearing motor was developed [4]. This motor was the combination of an AC motor and the hybrid AMB in which DC flux was used for the radial levitation control. Even though it could provide very stable levitation and strong rotating torque, again its size reduction was required for the application to the actual heart pump.

Aiming at small size, compactness and good efficiency as well as high performance, this paper introduces a hybrid-type short-span self-bearing motor. In this motor, a plate-shaped yoke is substituted for an AMB of the prior one, which results in a short rotor. Thus the rotor can be stably levitated by only two radial direction control, while the other motions become passively stable. In this paper, a mathematical model for the hybrid AMB part is built with consideration of the flux distribution in the circumferentially non-uniform air gap. Based on the model, a proportional and derivative (PD) controller for levitation is designed. To examine the performance of the proposed self-bearing motor, simple operation tests are carried out.

STRUCTURE OF THE NEW HYBRID-TYPE SELF-BEARING MOTOR
Figure 1(a) shows the usual hybrid-type self-bearing motor that consists of two parts; a self-bearing motor and an AMB. In the proposed self-bearing motor, the AMB part was substituted with a thin yoke as shown in Fig. 1(b). Note that the thin yoke can cause the saturation of bias flux, resulting in no radial destabilizing force acting on the yoke. It means that in such a way, the improved stability and efficiency of the system as well as the compact structure can be achieved. To reduce the size of whole system, the self-bearing motor was designed in the outer-rotor type. The stator has two kinds of winding; one is for levitation control and the other is for rotation. Figure 2(a) shows the stator with the general 8-pole 3-phase motor winding, and the cross-section of the rotor is represented in Fig. 2(b). Four thin PMs are attached on the inner surface of the rotor, which gives polarity of four pole-pair number.

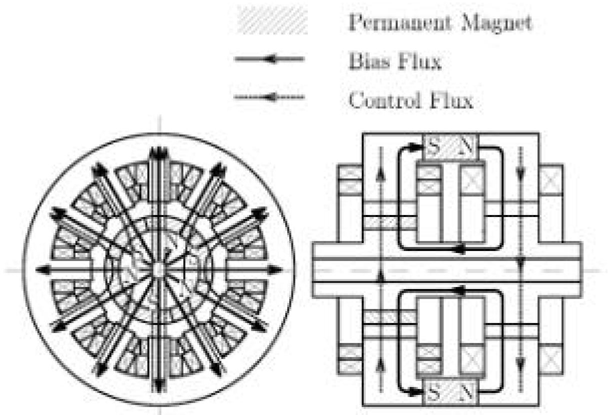

(a)

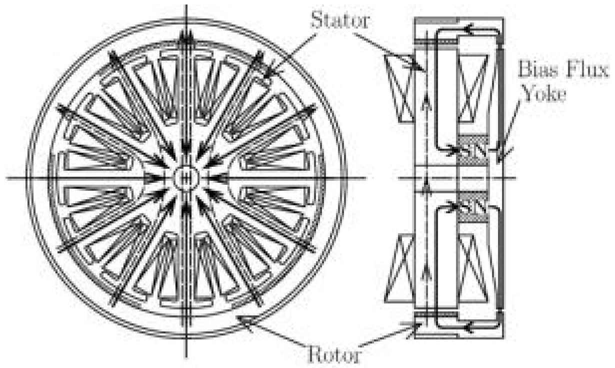

(b)

FIGURE 1: Schematics of (a) the conventional and (b) the proposed hybrid type self-bearing motor

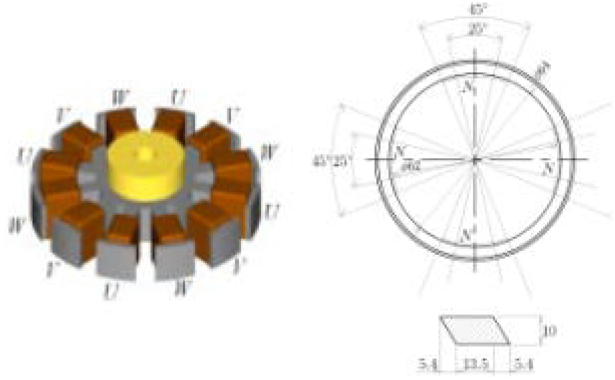

(a) (b)

FIGURE 2: (a) Stator with motor winding and a bias PM and (b) rotor with four thin PMs

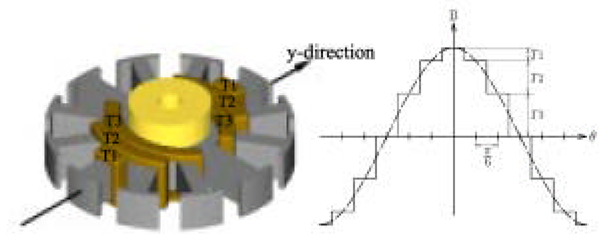

(a) (b)

FIGURE 3: (a) Stator with *y*-directional levitation winding and (b) the produced flux distribution

Notice that not S-pole PMs, but only N-pole ones are used, the structure of this motor part is not quite different from that of conventional PM motors. Figure 3 shows a set of two-pole levitation coil and the circumferential distribution of the flux density theoretically generated by the coil. There are two levitation coils in the stator at right angles with each other, just like the AMB.

As shown in Fig. 1(b), a PM located between the stator and the yoke produces the bias flux. It flows parallel to the rotor axis in the rotor and moves toward (or outward from) the center in the stator (or yoke). Meanwhile, control fluxes generated in levitation coils of the stator flow only on a plane perpendicular to the rotor axis, as depicted by the dotted line in the figure. Here, note that the control flux flowing over the air gap toward the center becomes added to the bias flux, which results in the increase of flux density or attractive force at that point, and vice versa. On the condition of uniform air gap, thus, Fig. 1(a) indicates that the upward magnetic force comes out. Based on this principle, a PD controller is designed so that the control flux can make the flux density in the wider air gap higher than that in the narrower, that is, so that the rotor can be stably levitated in radial direction.

RADIAL FORCE AND MOTOR TORQUE

Figure 4 shows the stationary coordinate system, where θ is the angular coordinate on the stator, M is the pole-pair number, and ω is the motor driving frequency. In our prototype, M is designed to be four. On the assumption that both stator and rotor are axi-symmetric and the air gap between them is circumferentially uniform, the flux densities in the air gap can be written as [4]

$$B_r = (B_0 + \frac{1}{2}B_1) + \frac{1}{2}B_1 \cos(M\theta - \omega t) \quad (1)$$

$$B_{sm} = B_2 \cos(M\theta - \omega t - \psi) \quad (2)$$

$$B_{sb} = B_3 \cos(\theta - \phi) \quad (3)$$

Here B_r, B_{sm} and B_{sb} are the flux densities generated by all PMs, motor coils and levitation coils, respectively; B_0 is the constant bias flux density; B_1 is the maximum flux density produced by the rotor magnets; B_2 and B_3 are the amplitudes of B_{sm} and B_{sb}, respectively; ϕ is the

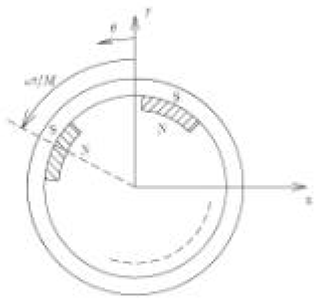

FIGURE 4: Coordinate system

phase of B_{sb}; ψ is the phase difference between B_r and B_{sm}. For convenience of calculation, the flux density produced by the rotor PMs is assumed to be sinusoidal. Therefore the total flux distribution B_g is given as

$$B_g = B_r + B_{sm} + B_{sb} \tag{4}$$

Now considering the magnetic energy stored in the air gap, we obtain the radial forces acting on the rotor as [4]

$$\begin{aligned} F_x &= \int_0^{2\pi} \frac{1}{2\mu_0} B_g^2 rl \cos\theta \, d\theta \\ &= \frac{\pi (B_0 + B_1/2) B_3 rl}{\mu_0} \cos\phi \qquad (when\ M \geq 3) \end{aligned} \tag{5}$$

$$\begin{aligned} F_y &= \int_0^{2\pi} \frac{1}{2\mu_0} B_g^2 rl \sin\theta \, d\theta \\ &= \frac{\pi (B_0 + B_1/2) B_3 rl}{\mu_0} \sin\phi \qquad (when\ M \geq 3) \end{aligned} \tag{6}$$

Here, F_x and F_y are the radial forces in the x and y direction, respectively; μ_0 is the permeability of free space; and r and l indicate the radius and length of the rotor, respectively. Equations (5) and (6) show that the radial forces depend only on B_3 and ϕ when $M \geq 3$. That is, the levitation control can be considered independently of the effect of the rotational flux field.
On the other hand, the motor torque T is calculated similarly as [4]

$$T = -\frac{\pi r g l B_1 B_2}{\mu_0} \sin\psi \qquad (when\ M \geq 2) \tag{7}$$

Likewise, the motor torque is determined by only B_2 and ψ, separately from the bias or levitation flux fields.
Figures 5 and 6 compare the measured and calculated data to validate the above expressions of F_x, F_y and T. In Fig. 5, the forces were measured as DC currents flowed in the levitation coil. Figure 6 shows the variation of the motor torque according to the change of ψ and motor current I_m. In both figures, regardless of many assumptions such as the axi-symmetry of rotor and

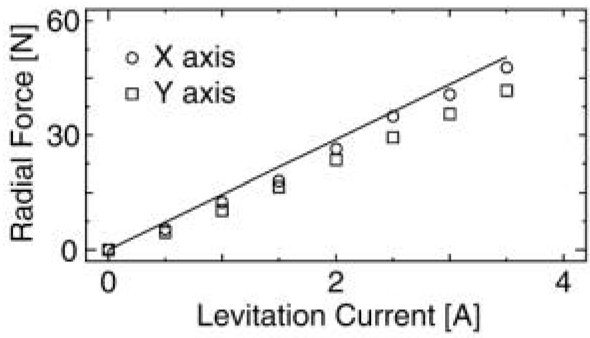

FIGURE 5: Radial forces: symbols are the measured data and solid line is the calculated result

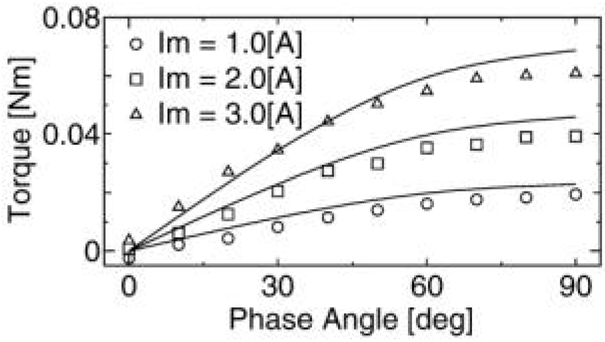

FIGURE 6: Motor torque: symbols are the measured data and solid lines are the calculated result

stator, uniform air gap, pure sinusoidal flux distribution, and no flux leakage, the results are quite reasonable.

MODELING OF THE HYBRID AMB PART

In general, Eqs. (5) and (6) are useful to simply estimate the radial force and the torque, or to find the minimum pole-pair number guaranteeing the independency of rotation and levitation. For the design of a levitation controller, however, it is needed to consider the rotor displacement on which the magnetic force is also largely dependent. In this section, the radial force generated by the hybrid AMB part is expressed as the function of rotor displacement and levitation current.

Bias Flux Densities

Let us suppose that in Fig. 4, the rotor moves in the y direction by $y(t)$. Then the air gap g_s on the stator side can be expressed as

$$g_s(y,\theta) = g_{s0} - y\cos\theta \tag{8}$$

where g_{s0} is the nominal air gap that includes the thickness of rotor PMs in view of bias flux. Since all bias fluxes flow across the air gap, the reluctance R_s can be regarded as connected in parallel. Thus

$$R_s = \left\{ \int \frac{\mu_0 dA_s}{g_s} \right\}^{-1} = \left\{ 2\mu_0 r l_s \int_0^{\pi} \frac{d\theta}{g_{s0} - y\cos\theta} \right\}^{-1} = \frac{\sqrt{g_{s0}^2 - y^2}}{\mu_0 A_s} \tag{9}$$

where l_s is the thickness of the stator, and A_s is the area of air gap ($=2\pi r l_s$). Note that the fringing effect and the effect of slots in the stator are neglected. Similarly, the reluctance R_y of the yoke-side air gap is

$$R_y = \frac{\sqrt{g_{y0}^2 - y^2}}{\mu_0 A_y} \tag{10}$$

where g_{y0} is the yoke-side nominal air gap, and A_y is the gap area. Assuming the core permeability is infinite, total reluctance R_T equals the sum of R_s and R_y; so

$$R_T = R_s + R_y \tag{11}$$

In general, the dc magnetization curve for a PM is represented as a straight line of the form

$$B_m = \mu_R H_m + B_r \tag{12}$$

where B_m and H_m are the flux density and the magnetic field intensity within the magnetic material, respectively, B_r is the residual flux density, and μ_R is the recoil permeability ($\approx \mu_0$). Recognizing that $\oint \boldsymbol{H} \cdot d\boldsymbol{l} = 0$ in this case, we can get

$$H_m l_m + H_s \sqrt{g_{s0}^2 - y^2} + H_y \sqrt{g_{y0}^2 - y^2} = 0 \tag{13}$$

where l_m is the length of bias PM, H_s and H_y are the magnetic field intensities in the stator-side and the yoke-side air gap, respectively. Since the total bias flux ϕ_B must be continuous through the magnetic circuit, therefore

$$\phi_B = A_m B_m = A_s B_s^* = A_y B_y^* \tag{14}$$

where A_m is the area of bias PM, and B_s^* ($=\mu_0 H_s$) and B_y^* ($=\mu_0 H_y$) are the averaged flux densities in the gaps, generated by the bias PM. From Eqs. (12), (13) and (14), ϕ_B is given by

$$\phi_B = \frac{B_r}{\dfrac{1}{A_m} + \dfrac{\mu_R}{\mu_0}\left\{ \dfrac{\sqrt{g_{s0}^2 - y^2}}{l_m A_s} + \dfrac{\sqrt{g_{y0}^2 - y^2}}{l_m A_y} \right\}} \tag{15}$$

Then the flux $d\phi_B$ passing through the infinitesimal section at the θ angular position can be expressed as

$$d\phi_B = \frac{R_s}{R_s|_{d\theta}} \phi_B \equiv B_s(\theta) dA_s \tag{16}$$

where $R_s|_{d\theta} = \dfrac{g_{s0} - y\cos\theta}{\mu_0 dA_s}$ is the reluctance of the infinitesimal section and B_s is the flux density distribution in the stator-side air gap. By using Eqs. (9) and (16), we obtain

$$B_s(\theta) = \frac{\sqrt{g_{s0}^2 - y^2}}{A_s(g_{s0} - y\cos\theta)} \phi_B \tag{17}$$

Similarly, in the yoke-side air gap,

$$B_y(\theta) = \frac{\sqrt{g_{y0}^2 - y^2}}{A_y(g_{y0} - y\cos\theta)} \phi_B \tag{18}$$

Note that for the saturation of B_y at all times, its minimum value, i.e. the case of θ = 180° and y = touchdown gap, must be over the saturation flux density of core material.

Flux Density by Levitation Coil

Referring to Fig. 3, the control flux paths induced by y-direction displacement have symmetry for the x axis, but only with the opposite direction. Assuming the air gap within a pole is uniform, we can express the reluctance R_{T1} for the flux path made by two T_1-turn windings as

$$R_{T1} = \frac{2g_{s0}}{\mu_0 A_p} \tag{19}$$

where A_p is the area of a pole ($A_p \approx A_s/12$). Note that R_{T1} is constant regardless of y. The flux density B_{T1} produced by the T_1-turn windings is given as

$$B_{T1} = \frac{2T_1 i_y}{R_{T1} A_p} = \frac{\mu_0 T_1 i_y}{g_{s0}} \tag{20}$$

where i_y is the y-directional control current.

In similar way, the flux densities B_{T2} and B_{T3} generated by the T_2 and T_3-turn windings, respectively, can be written as

$$B_{T2} = \frac{\mu_0 T_2 i_y}{g_{s0}} \tag{21}$$

$$B_{T3} = \frac{\mu_0 T_3 i_y}{g_{s0}} \tag{22}$$

As disregarding the fringing effect, the control flux densities driven above are not related to the rotor displacement.

Radial Force

From Eqs. (10) and (15), the y-direction radial force F_{yoke} acting on the rotor in the yoke part is given by

$$F_{yoke} = -\frac{1}{2} f_B^2 \frac{dR_y}{dy}$$

$$= \frac{\dfrac{B_r^2 y}{\sqrt{g_{y0}^2 - y^2}}}{2m_0 A_y \left[\dfrac{1}{A_m} + \dfrac{m_R}{m_0} \left\{ \dfrac{\sqrt{g_{s0}^2 - y^2}}{l_m A_s} + \dfrac{\sqrt{g_{y0}^2 - y^2}}{l_m A_y} \right\} \right]^2} \tag{23}$$

And on the stator side, from Eqs. (17), (20), (21) and (22), the y-direction radial force F_{stator} is

$$F_{stator} = \frac{B_r^2 y}{\dfrac{m_0 A_s^2}{g_{s0} A_p} \left[\dfrac{1}{A_m} + \dfrac{m_R}{m_0} \left\{ \dfrac{\sqrt{g_{s0}^2 - y^2}}{l_m A_s} + \dfrac{\sqrt{g_{y0}^2 - y^2}}{l_m A_y} \right\} \right]^2}$$
$$\times \left\{ \frac{2}{g_{s0}^2 - y^2} + \frac{3\left(g_{s0}^2 - y^2\right)}{\left(g_{s0}^2 - 3y^2/4\right)^2} + \frac{g_{s0}^2 - y^2}{\left(g_{s0}^2 - y^2/4\right)^2} \right\}$$
$$+ \frac{2 i_y B_r \sqrt{g_{s0}^2 - y^2}}{\dfrac{A_s}{A_p} \left[\dfrac{1}{A_m} + \dfrac{m_R}{m_0} \left\{ \dfrac{\sqrt{g_{s0}^2 - y^2}}{l_m A_s} + \dfrac{\sqrt{g_{y0}^2 - y^2}}{l_m A_y} \right\} \right]}$$
$$\times \left\{ \frac{T_1 + T_2 + T_3}{g_{s0}^2 - y^2} + \frac{\sqrt{3}\left(T_2 + T_3\right)}{g_{s0}^2 - 3y^2/4} + \frac{T_3}{g_{s0}^2 - y^2/4} \right\} \tag{24}$$

Thus the total y-direction force F_y is

$$F_y = F_{stator} + F_{yoke} \tag{25}$$

Note that F_y is in direct proportion to the control current i_y. In practice, however, un-modeled effects such as fringing effect and flux leakage may cause high order terms of i_y in Eq. (24). Also, since neglecting the radial destabilizing force generated by the rotational flux field, the model may have some inaccuracy.

LEVITATION CONTROLLER DESIGN

Linearization of Force

In order to design a PD controller, the force equation in Eq. (25) is linearized. Assume that y is much smaller than g_{s0} and g_{y0}, and then, by using the Taylor series expansion,

$$F_y \approx \left.\frac{\partial F_y}{\partial y}\right|_{y, i_y = 0} y + \left.\frac{\partial F_y}{\partial i_y}\right|_{y, i_y = 0} i_y \equiv K_y y + K_i i_y \tag{26}$$

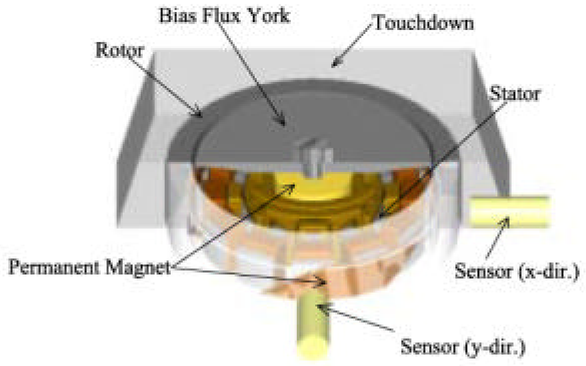

FIGURE 7: Schematic of the experimental setup

where

$$K_y = \frac{\left(g_{s0} A_s + g_{y0} A_y\right) B_r^2}{2 m_0 g_{s0} g_{y0} A_s A_y \left\{ \dfrac{1}{A_m} + \dfrac{m_R}{m_0 l_m} \left(\dfrac{g_{s0}}{A_s} + \dfrac{g_{y0}}{A_y} \right) \right\}^2} \tag{27}$$

$$K_i = \frac{\left\{ T_1 + (1+\sqrt{3}) T_2 + (2+\sqrt{3}) T_3 \right\} B_r}{6 g_{s0} \left\{ \dfrac{1}{A_m} + \dfrac{m_R}{m_0 l_m} \left(\dfrac{g_{s0}}{A_s} + \dfrac{g_{y0}}{A_y} \right) \right\}} \tag{28}$$

Simplest PD Controller

Neglecting all time constants of the control loop, the 1-d.o.f. equation of motion and controller equation are reduced as

$$m\ddot{y} - K_y y = K_i i_y \tag{29}$$

$$i_y = -K_s K_A \left(K_p y + K_d \dot{y}\right) \tag{30}$$

where m is the mass of rotor, K_s and K_A are the gains of sensor amplifier and power amplifier, respectively, K_p and K_d are the P- and D-gains of controller, respectively. The control gains can be simply obtained as [5]

$$K_p = \frac{m w_n^2 + K_y}{K_s K_A K_i} \quad \text{and} \quad K_d = \frac{2 m z w_n}{K_s K_A K_i} \tag{31}$$

where w_n and z are the desired natural frequency and damping coefficient of the system, respectively.

EXPERIMENT

Figure 7 shows the experimental setup, in which two gap sensors are equipped to measure the x and y displacements of the rotor, and a touchdown plate limits the rotor motion to half of air gap. In order to reduce the eddy current effect, the stator is laminated with silicon steel plate. The design parameters are listed in Table 1. Figure 8 shows the schematic diagram of the control

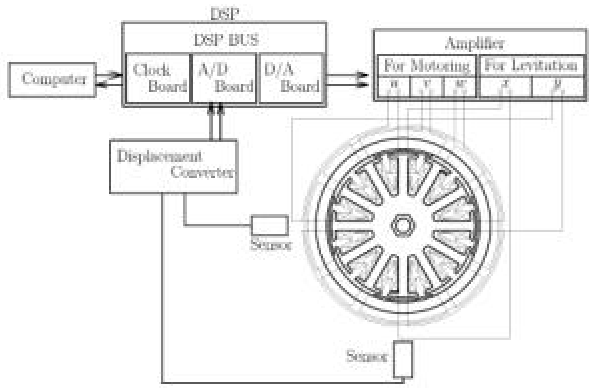

FIGURE 8: Schematic of the control system

system. The rotor displacements measured by two gap sensors are transformed into a digital signal processor (DSP; TMS320C40) to generate proper control signals. The control signals are fed to each power amplifier, resulting in the currents of levitation coils.

Figure 9 shows the experimental results; unbalance responses and axial-direction rotor motions. The rotor could run up to 3,700 rpm. Below 3000 rpm, the amplitude of radial vibration was kept within 0.015 mm. While, the axial-direction vibration was relatively large. Making allowance for the first trial setup, these results indicate the enough possibility of the proposed system.

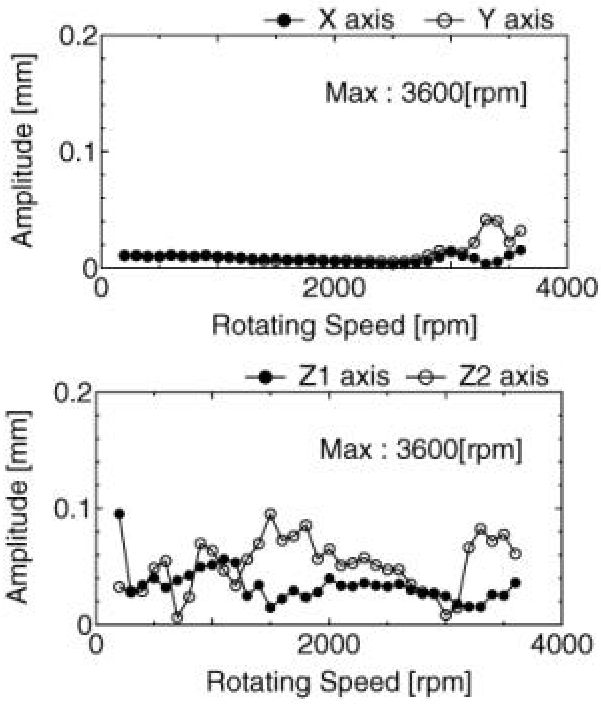

FIGURE 9: Sizes of radial and axial vibration when motor current is 2.0 [A]

CONCLUSION

A new hybrid type self-bearing motor, which is composed of a self-bearing motor and a yoke, was introduced. The thin yoke yielded a short rotor, which resulted in not only small size but also simplified control mechanism due to the passive stability for the axial and tilting motion. A mathematical model was built to design the levitation controller. Through simple operation tests, the control gains chosen based on the model were proved to be well-designed for the stable levitation. In conclusion, the experimental results showed the feasibility of the proposed self-bearing motor system for use in an artificial heart.

Further work will be continued to get the improved stability and efficiency by using the saturation of flux density in the yoke-side air gap.

TABLE 1: Design parameters

Parameter	*Value*	*Parameter*	*Value*
Outer dia. (rotor)	74 mm	Motor coil (3-phase 8-pole)	50 turns per pole
Rotor length	20.5 mm		
Diameter (stator)	62 mm	Levitation coils (T_1, T_2, T_3)	15,41,56 turns
Air gap, g_{s0}	2 mm		
Air gap, g_{y0}	1 mm	Coil diameter	0.5 mm
Area of gap, A_s	1524mm^2	Sampling time	0.1 msec
Area of gap, A_y	283 mm^2	Sensor amp. gain	2.5V/mm
Bias PM length	7 mm	Power amp. gain	0.5 A/V
Bias PM area, A_m	286 mm^2	P gain, K_p	20
Rotor PM thick.	1 mm	D gain, K_d	0.02
Rotor PM area	189 mm^2	K_y [N/mm]	145.6
B_r of all PMs	1.3 Tesla	K_i [N/A]	7.57

REFERENCES

1. Okada Y. et al., Levitation and Torque Control of Internal Permanent Magnet Type Bearingless Motor, IEEE Trans. on Control System Tech., 4(5), 1996, pp. 565-570.
2. Oshima et al., Characteristics of a Permanent Magnet Type Bearingless Motor, Proc. 1994 IEEE IAS, 1, Denver, CO, 1994, pp. 196-201.
3. Schöb R. and Barletta N., Principle and Application of a Bearingless Slice Motor, Proc. of 5th ISMB, Kanazawa, Japan, 1996, pp. 313-318.
4. Okada Y. et al., Hybrid AMB Type Selfbearing Motor, Proc. of 6th ISMB, MIT, Cambridge, MA, USA, 1998, pp. 497-506.
5. Schweitzer G. et al., Active Magnetic Bearings, Hochschulverlag AG as der ETH Zürich, 1994.